Materials Today Chemistry 24 (2022) 100896

Contents lists available at ScienceDirect

Materials Today Chemistry

journal homepage: www.journals.elsevier.com/materials-today-chemistry/

Flexible carbon membrane supercapacitor based on γ-cyclodextrin-MOF☆

W. Xu [a, b], Li-H Wang. [a, b], Y. Chen [a, b, *], Y. Liu [a, b, **]

[a] College of Chemistry, State Key Laboratory of Elemento-Organic Chemistry, Nankai University, Tianjin, 300071, PR China
[b] Haihe Laboratory of Sustainable Chemical Transformations, Tianjin, 300192, PR China

ARTICLE INFO

Article history:
Received 10 January 2022
Received in revised form
4 March 2022
Accepted 12 March 2022
Available online xxx

Keywords:
Electrospun carbon fibers
High energy density
Supramolecular porous structure
Electrode

ABSTRACT

Supercapacitors (SCs) with high energy density and power density are a research hotspot. Herein, we report a flexible porous carbon membrane supercapacitor prepared by electrospinning polyacrylonitrile (PAN) with γ-cyclodextrin-MOF (γ-CD-MOF) and then carbonizing at 900 °C. BET results showed that the supercapacitor retained the skeleton of γ-CD, γ-CD-MOF and the pores formed by the spun-fibers, which were 0.73, 1.09 and 23−186 nm, respectively, showing a high specific surface area of 134.7 m^2/g. The hierarchically porous structures ensure rapid charge transfer and ion diffusion, resulting in the PAN/γ-CD-MOF carbon electrode with a high capacity of 283.3 F/g. Moreover, the supercapacitor had a high energy density up to 17.5 Wh/kg and power density up to 6 kW/kg. Significantly, it showed excellent cycle stability with a capacitance retention of 97.5% after 6000 cycles. This work provides a supramolecular strategy to construct a flexible porous carbon membrane, which has potential for supercapacitor applications.

1. Introduction

Supercapacitors (SCs) have become a research hotspot because of their applications in many fields, including intelligent textiles [1], wearable electronics [2,3], portable devices [4], wireless charging storage devices [5,6], and implantable medical electronics [7]. SCs have the characteristics of fast charge and discharge capabilities, high power density and long cycle life [8]. However, there is still a challenge to improve the energy density of SCs (approximately 10 Wh/kg for the best commercial devices) [9]. Increasing the capacitance of electrode materials and broadening their potential window are effective means to improve energy density.

Supramolecular assembly strategies have been very popular in recent years, and can be used in various fields including chiral selectivity [10,11], light-harvesting systems [12], 3D printing [13], drug carriers [14,15] and supercapacitors [16]. Kim reported a stretchable, self-healable, and photodegradable supercapacitor using an Azo-PAM/α-CDP/LiCl hydrogel as polyelectrolyte [17]. We used 6-acrylamidomethylether-modified α-CD and PEG (20,000) diacrylate to construct a polypseudorotaxane. Then, the polypseudorotaxane reacted with acrylamide via photo-initiated polymerization in situ. After doping ions, a slide-ring hydrogel stretchable and compressible supercapacitor was obtained [18]. Recently, we reported several flexible conductive electrodes constructed by loading zinc-based metal organic framework (MOF) (ZIF-8) onto a carbon nanotube film (CNTF) and further electrically depositing macrocycles and conductive polymers (CPs) [19].

A chemical structure with an ordered porous skeleton that is conducive to high charge transfer efficiency is of great significance for the construction of supercapacitors with increased capacitance [20]. Therefore, MOFs have become promising materials for SCs because of their ordered structure, large specific surface area, and controllable pore size distribution [21]. However, the main obstacles that seriously limit the use of MOFs in practical electrochemical applications are their limited conductivity, low chemical stability and poor mechanical properties [22]. To meet this challenge, MOFs have been used as attractive precursors for fabricating carbon-based nanomaterials [23]. Cheng reported ZIF-8/graphene/CNT-derived carbon frameworks with a continuous conductive network, porous structure, and abundant nitrogen doping [21]. Conductive porous carbon has the advantages of low cost, good

☆ Dedicated to Sir Fraser Stoddart on the occasion of his 80th birthday.

* Corresponding author.
** Corresponding author.
E-mail addresses: chenyong@nankai.edu.cn (Y. Chen), yuliu@nankai.edu.cn (Y. Liu).

https://doi.org/10.1016/j.mtchem.2022.100896
2468-5194/

chemical, mechanical and thermal stability, high conductivity and enables fast access by electrons and ions [24,25].

Most SCs stick the active powder to the electrode through binders, which increases the preparation cost as well as the interfacial resistance. Moreover, the active powder easily agglomerates in the process of electrochemical reaction, resulting in relatively poor cycle stability [26]. Therefore, freestanding flexible porous membranes are highly desired. Sarno et al. prepared a compact and porous PVDF-HFP-MoS_2 (PVMS) supercapacitor using a supercritical—CO_2—assisted gel drying process [27]. A porous poly(-vinylidene fluoride) (PVDF) membrane was prepared via a phase-inversion method followed by polarization to induce piezoelectricity. Then the PVDF membrane was employed as supercapacitor separators for reduced self-discharge [28]. By using poly(ionic liquid) membranes as pyrolysis precursor, Zhang et al. fabricated binder-free B,N-co-doped nano-porous carbon membranes [29]. Electrospinning technology has great advantages in constructing freestanding flexible porous carbon membranes, which are conducive to rapid mass transfer and reduce resistance [30]. Fiberous supercapacitors are favored because of their flexibility, light weight and high porosity. However, due to the slow diffusion and storage of ions in compacted fibers, achieving high energy density is still a challenge [20].

In view of the above, there are few reports on constructing flexible self-supporting SCs with high energy density using a supramolecular assembly strategy. In particular, electrospun supercapacitors with supramolecular macrocycles have not been reported, to the best of our knowledge. Here, we report a nanofibrous membrane constructed by co-spunning PAN and γ-CD-MOF, carbonizing the membrane, and separating the fibers by γ-CD-MOF so that they would not be stacked too tightly. It is a simple and easy method to prepare layered freestanding flexible porous carbon membranes with ordered structures (Fig. 1).

2. Results and discussion

2.1. Characterization of γ-CD-MOF

The specific steps of synthesizing γ-CD-MOF are described in the experimental section. The microscopic morphology of γ-CD-MOF is shown in Fig. 2a and b. Scanning electron microscope (SEM) and transmission electron microscope (TEM) images show that γ-CD-MOF is a square structure with a size of approximately 200 nm, that is uniform in size and regular in shape. The powder X-ray diffraction (XRD) pattern (Fig. 2c) of the synthesized γ-CD-MOF manifests high crystallinity and is the same as the reported pattern, indicating

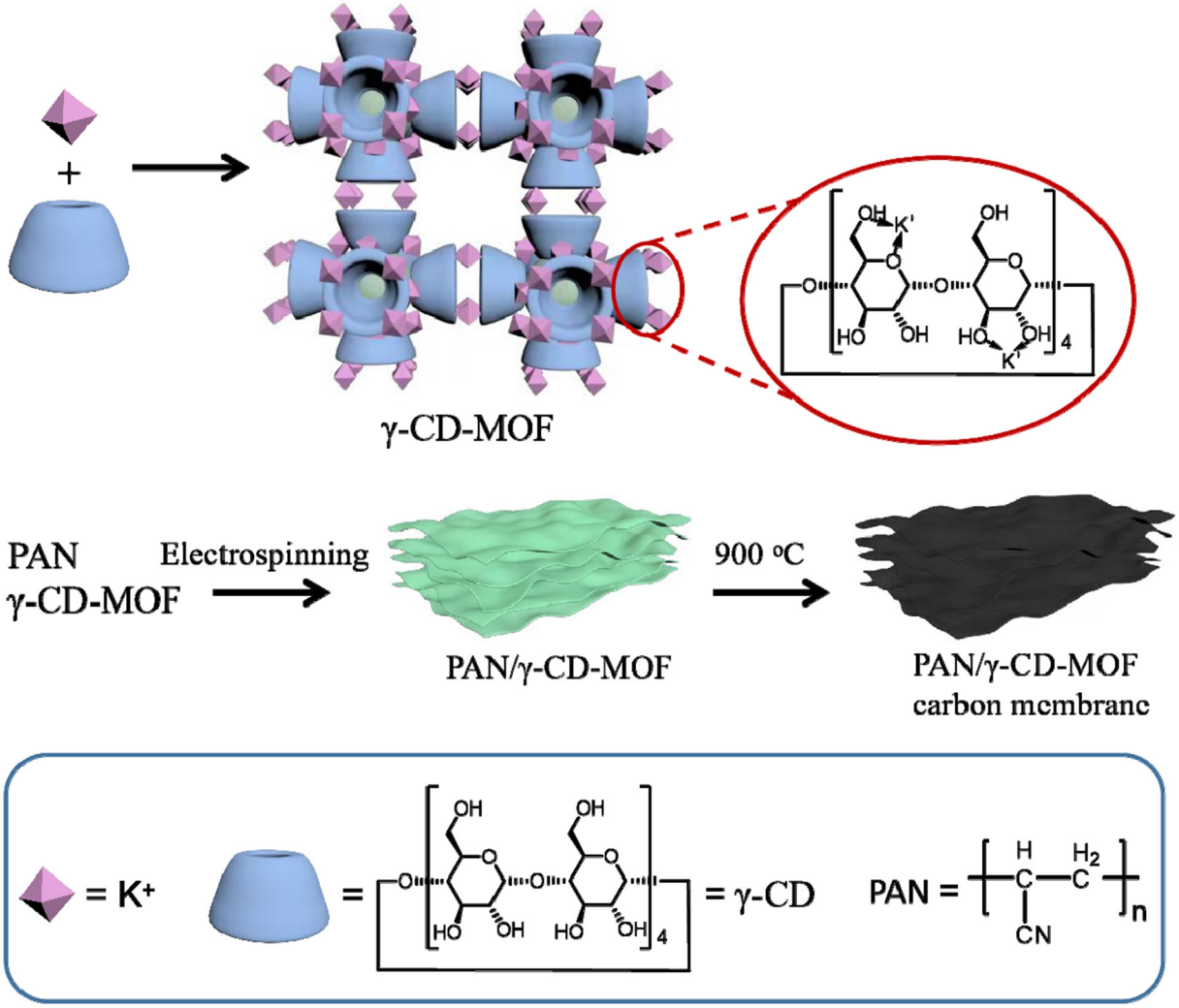

Fig. 1. Schematic diagram of the PAN/γ-CD-MOF carbon membrane prepared by electrospinning.

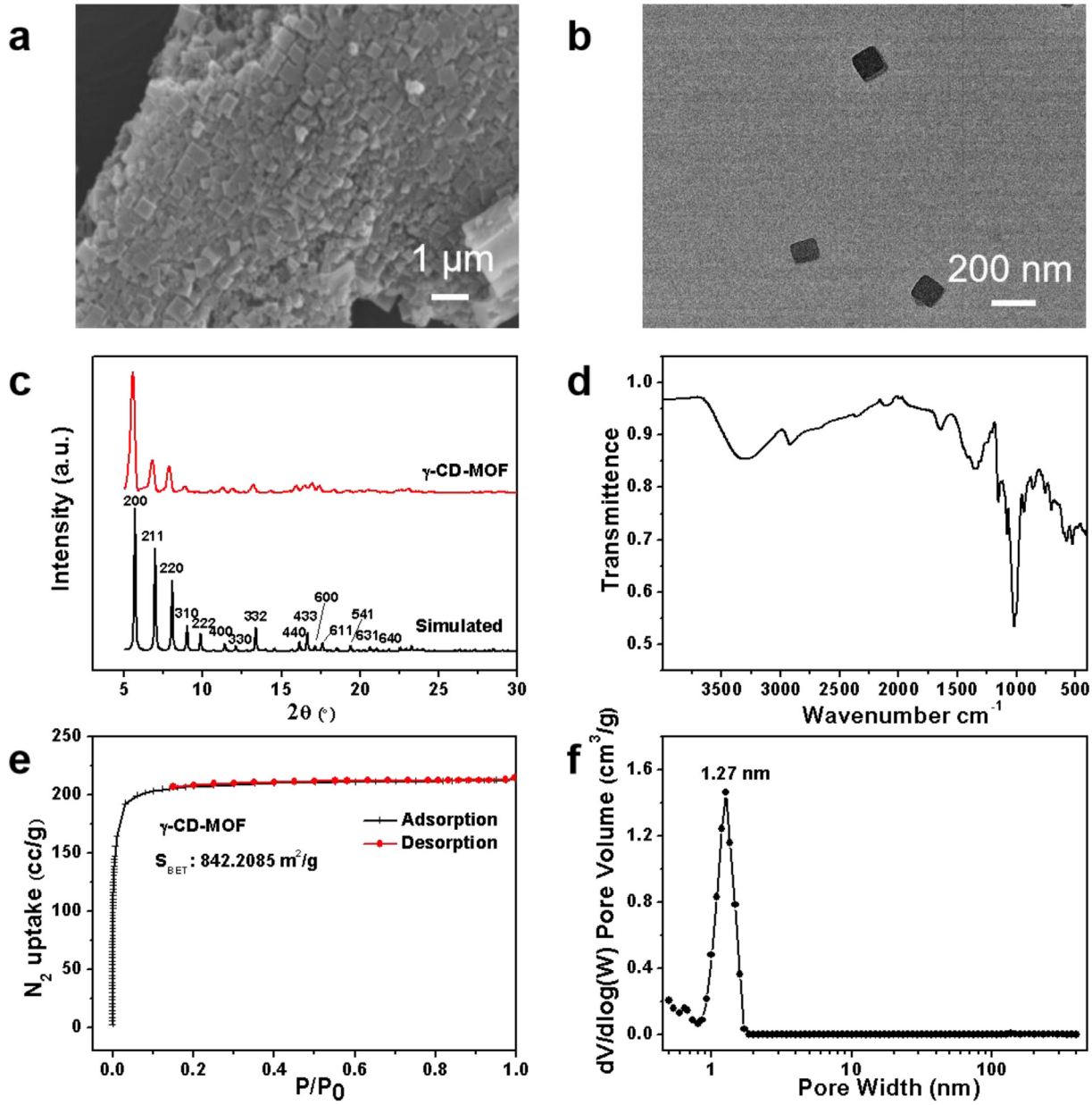

Fig. 2. Characterization of γ-CD-MOF. (a) SEM image, (b) TEM image, (c) Simulated crystallographic diffraction pattern of γ-CD-MOF based on single-crystal structure from the Cambridge structural database, and X-ray powder diffraction patterns of the prepared γ-CD-MOF, (d) FT-IR spectrum, (e) N_2 adsorption/desorption isotherm, and (f) pore-size distribution.

the formation of a cubic framework [31,32]. Comparing the X-ray powder diffraction pattern of the as-prepared γ-CD-MOF with the simulated crystallographic diffraction pattern of γ-CD-MOF, the results show that all the peaks in the XRD pattern are indexed to the phase of γ-CD-MOF [33].

The Fourier transform infrared spectroscopy (FT-IR) spectrum of γ-CD-MOF (Fig. 2d) shows a broad absorption peak at 3301 cm^{-1} assigned to the −OH group stretching vibrations. The peak at 2919 cm^{-1} originates from the stretching vibrations of C−H bonds from the $-CH_2$ and −CH groups. The peaks at 1644, 1421 and 1152 cm^{-1} are attributed to −OH group bending vibrations. The peak at approximately 1027 cm^{-1} is assigned to the stretching vibration of the C−O−C bond. The peak at 863 cm^{-1} corresponds to the C−C stretching vibrations [34−36]. The N_2 adsorption/desorption isotherms of γ-CD-MOF (Fig. 2e) exhibit typical type-I physisorption behavior and a sharp rise at a low relative pressure, which is characteristic of microporous materials. The Brunauer-Emmett-Teller (BET) specific surface area of the γ-CD-MOF was found to be 842.2 m^2/g, and the micropore volume was 0.32 cm^3/g. Pore size distributions (Fig. 2f) indicated that the measured γ-CD-MOF mainly contained micropores at 1.27 nm. Energy dispersive X-ray spectroscopy (EDS) elemental analysis (Supplementary Fig. 1) proves that γ-CD-MOF contains carbon, oxygen, and potassium elements, and the mapping images confirm (Supplementary Fig. 2) the homogeneous distribution of these elements.

2.2. Characterization of PAN/γ-CD-MOF electrospun membrane

PAN and PAN/γ-CD-MOF nanofibrous membranes were prepared by electrospinning technology. SEM images (Supplementary

Fig. 3) showed that the PAN nanofibers were uniformly distributed, but PAN/γ-CD-MOF showed a few nodules in the nanofibers, meaning that γ-CD-MOF nanoparticles were well dispersed in PAN at a high loading efficiency of 50 wt % (content relative to polymer). The average diameters of the nanofibers in the PAN and PAN/γ-CD-MOF membranes were approximately 260 and 390 nm, respectively. Elemental analysis (Supplementary Fig. 4) proved that PAN contains C and N elements, while PAN/γ-CD-MOF contains C, N, O and K elements. TEM (Supplementary Fig. 5) also confirmed that the size of PAN/γ-CD-MOF was about 400 nm. In the FT-IR spectra of the PAN and PAN/γ-CD-MOF nanofibrous membranes (Supplementary Fig. 6), the peak at 2243 cm^{-1} was assigned to the cyano group (-CN), and the peaks at 2938, 1452, and 1227 cm^{-1} were ascribed to stretching vibration and bending vibration of $-CH_2$, as well as left-right swing vibration of −CH, respectively, indicating the successful construction of PAN nanofibers [37,38]. In addition to the characteristic absorption peaks of PAN, the FT-IR spectrum of the PAN/γ-CD-MOF membrane presented peaks of γ-CD-MOF at 3355 cm^{-1} (belonging to the stretching vibration peak of −OH) and in the 1200-1000 cm^{-1} region (characteristic of the glucose ring), indicating that γ-CD-MOF was contained in the PAN/γ-CD-MOF membrane. Aiming to obtain a carbon-rich porous flexible membrane, we therefore studied the weight loss of PAN and PAN/γ-CD-MOF under a N_2 atmosphere through a thermogravimetry device. The thermal gravimetric analysis (TGA) traces are shown in Supplementary Fig. 7. For the PAN membrane, the initial weight loss below 300 °C was attributed to solvent evaporation. Consistent with previous reports, PAN decomposition occurred mainly in three temperature ranges: 300, 300−500, and >500 °C, corresponding to three chemical reactions: cyclization, carbonization, and thermal oxidation [37]. The shape of the TGA curve of PAN/γ-CD-MOF is basically similar to that of PAN, however, after solvent loss, the thermal degradation of PAN/γ-CD-MOF occurred at temperatures over 200 °C due to the existence of γ-CD-MOF [39]. It

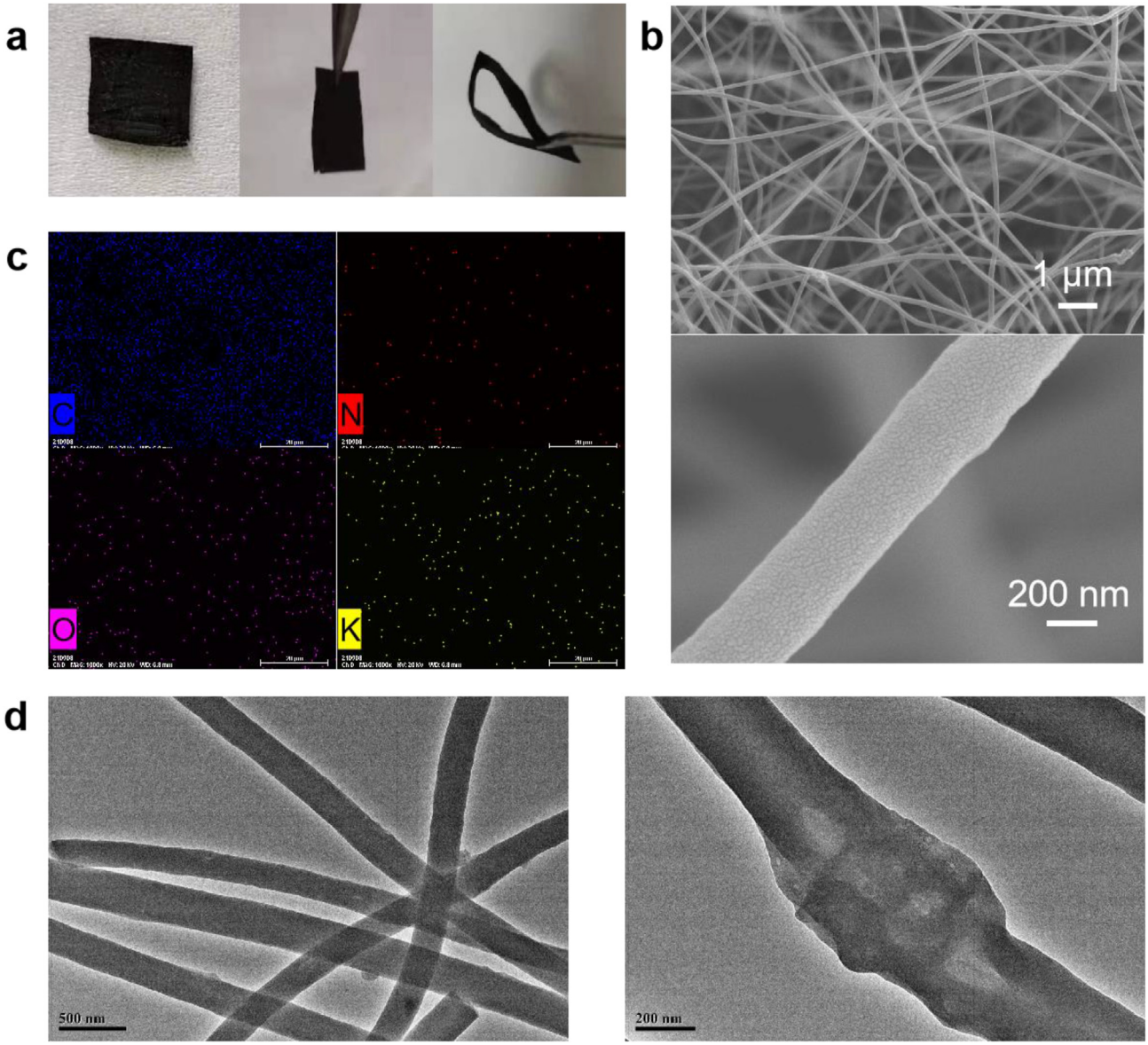

Fig. 3. Characterization of PAN/γ-CD-MOF carbon membrane. (a) Photographs and flexibility demonstrations, (b) SEM images, (c) EDS elemental mapping analysis, and (d) TEM images.

is important that the total carbon yield was 31.9% according to TGA, proving that a carbon-rich porous flexible membrane can be obtained after 900 °C carbonization.

2.3. Characterization of PAN/γ-CD-MOF electrospun carbon membrane

To increase its conductivity, the PAN/γ-CD-MOF electrospun membrane was programmed to heat up to 900 °C for carbonization in a nitrogen atmosphere with a constant flow rate of 0.01 L/min. As shown in Fig. 3a, a flexible carbon membrane was obtained after carbonization, which would not be broken even when it was folded and bent. SEM (Fig. 3b and Supplementary Fig. 8) showed that the average diameter of the nanofibers in the PAN/γ-CD-MOF carbon membrane was approximately 240 nm. Elemental analysis (Fig. 3c and Supplementary Fig. 9) proved that the PAN/γ-CD-MOF carbon membrane contains C, N, O and K elements, and mapping images confirmed the homogeneous distribution of these elements. To the best of our knowledge, there are no reports on the reaction of PAN or γ-CD-MOF with N_2 in the temperature range from room temperature to 900 °C. Elemental analyses of the PAN/γ-CD-MOF nanofibrous membrane before and after carbonization were performed, and the test data were supplemented in Supplementary Table 1. The results showed that the nitrogen content decreased significantly from 19.26% to 10.83% after heat treatment, which may prove that N_2 gas did not participate in the reaction at high temperature.

TEM (Fig. 3d) also confirmed that the diameter of the nanofibers in the PAN/γ-CD-MOF carbon membrane was approximately 240 nm. When γ-CD-MOF aggregates, bulges appear on the nanofibers. Some bulges appeared on both the SEM image of Fig. 3b and the TEM image of Fig. 3d, indicating that γ-CD-MOF was slightly aggregated.

N_2 adsorption-desorption isotherms of the PAN/γ-CD-MOF carbon membrane (Fig. 4a) increased sharply at low relative pressures and high relative pressures, indicating major microporous and macropore features, respectively. Meanwhile, hysteresis occurred under medium relative pressure conditions, indicating the presence of mesopores. Attributed to the abundance of micropores, mesopores and macropores, as confirmed from the N_2 sorption isotherms, the PAN/γ-CD-MOF carbon membrane has a high surface area of 134.7 m^2/g, with a pore size distribution of micropores at 0.73 and 1.09 nm, as well as mesopores and macropores from 23 to 186 nm (Fig. 4b), which undoubtedly promotes ion dynamics, shortens the mass transfer distance and facilitates charge storage. The graphitization degree of the PAN/γ-CD-MOF carbon membrane was tested by Raman spectroscopy (Fig. 4c). Two peaks located at 1342 cm^{-1} and 1581 cm^{-1} belonged to the D-band and G-band, which represented disordered carbon and ordered graphite crystalline structures, respectively [20,40]. The broad peak appearing between 2500 and 3000 cm^{-1} was attributed to the 2D-band, indicating layered carbon structures [24,41]. A high degree of graphitization indicates that the material has good conductivity. After connecting the PAN/γ-CD-MOF carbon membrane to the circuit as a part of the wire, the bulb can be lit, demonstrating the good conductivity of the PAN/γ-CD-MOF carbon membrane (Fig. 4d).

As shown in Supplementary Fig. 10, the XRD pattern of the PAN membrane had a diffraction peak at $2\theta = 17°$ assigned to (100)

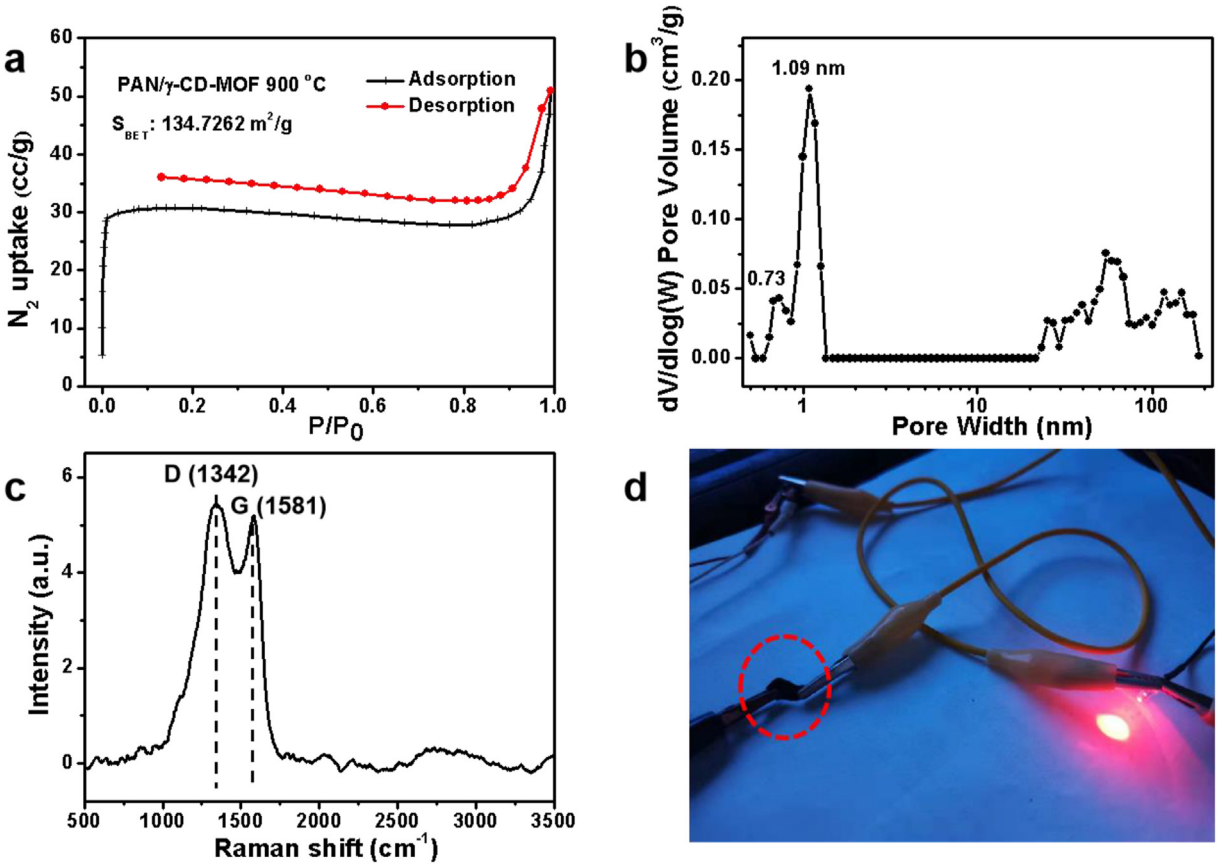

Fig. 4. Characterization of PAN/γ-CD-MOF carbon membrane. (a) N_2 adsorption/desorption isotherm, (b) pore-size distribution, (c) Raman spectrum, and (d) photograph of using the PAN/γ-CD-MOF carbon membrane as a wire to light up the bulb.

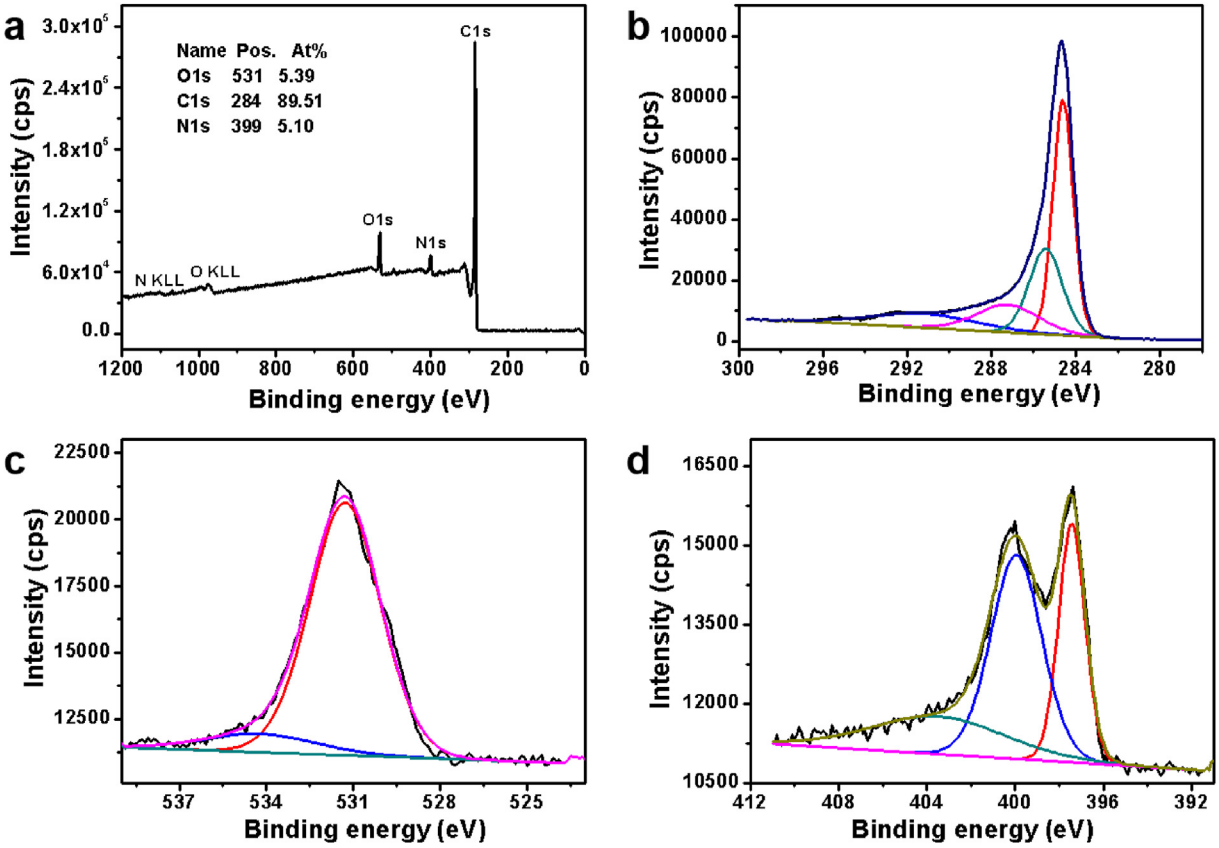

Fig. 5. XPS of PAN/γ-CD-MOF carbon membrane. (a) XPS spectrum, (b) XPS C 1s spectra, (c) XPS O 1s spectra, and (d) XPS N 1s spectra.

crystal plane diffraction and a characteristic diffraction peak at $2\theta = 29^\circ$ assigned to the (110) crystal plane of the cyano group [37]. The characteristic diffraction peaks of PAN/γ-CD-MOF were very similar to those of PAN, implying that the original PAN structure was preserved, but the peak strength was weakened compared with that of PAN. Because γ-CD-MOF was spun into the PAN fibers, its characteristic diffraction peaks were not observed. Two broad diffraction peaks appearing at $2\theta = 23^\circ$ and 44° in the XRD spectrum of the PAN/γ-CD-MOF carbon membrane were assigned to the (002) and (101) crystal planes of graphitic carbon, indicating a high graphitization degree of the carbon membrane, and the (002) peak of graphite represents the characteristic π-π stacked layers [20,42].

X-ray photoelectron spectroscopy (XPS) measurements were used to investigate the chemical compositions of the PAN/γ-CD-MOF carbon membrane surface (Fig. 5), presenting the existence of C (284 eV), N (399 eV) and O (531 eV) elements (Fig. 5a). The C1s spectrum (Fig. 5b) showed four peaks at 284.6, 285.4, 287.2 and 291.2 eV, assigned to C–C/C=C, C–O, C=O/C=N and O–C=O species, respectively. The high resolution O1s spectrum (Fig. 5c) exhibited two peaks at 531.3 and 534.2 eV, corresponding to C=O and C–O species. The N1s signal (Fig. 5d) showed three peaks at 397.4, 399.9 and 403.5 eV, assigned to pyridinic-type N, pyrrolic-type N, and N–O species, respectively [22,40]. It is noteworthy that the introduction of foreign atoms such as N and O can adjust the specific surface area and electronic properties of carbon materials [43]. Furthermore, heteroatom doping can also broaden the potential window of water-based supercapacitors and improve their charge storage performance, leading to increased specific capacitance [40].

2.4. Electrochemical performance of PAN/γ-CD-MOF carbon membrane electrode

Compared with organic electrolytes, aqueous electrolytes have the advantages of good security, low cost and strong operability in ordinary environments [44]. Traditional organic electrolytes are flammable and volatile, which may cause fire or explosion [45]. Relatively speaking, aqueous electrolytes have better security.

To evaluate the electrochemical performance of the PAN/γ-CD-MOF carbon membrane electrode, we conducted electrochemical impedance spectroscopy (EIS), cyclic voltammetry (CV), and galvanostatic charge and discharge (GCD) measurements in 1 M H_2SO_4 with a three-electrode system, using Ag/AgCl as the reference electrode, to estimate the specific capacitance of the PAN/γ-CD-MOF carbon membrane as the supercapacitor electrode material. EIS was performed to evaluate ion diffusion and storage. The intersection of the high frequency curve and the horizontal axis represents the resistance of the electrolyte; the diameter of the semicircle at high frequency clarifies the charge-transfer resistance inside the electrode; and the slope of the straight line at low frequency reveals the ion diffusion ability [46]. The EIS data (Fig. 6a) showed that both the electrolyte resistance and the charge-transfer resistance were at low values, and the straight line in the low frequency region indicated high ionic accessibility. CV curves of the PAN/γ-CD-MOF carbon membrane electrode were collected at scan rates ranging from 5 to 500 mV/s. The PAN/γ-CD-MOF carbon membrane electrode was found to be electrochemically stable when swept in the potential range of −0.2 to 1.0 V (versus Ag/AgCl) as seen from Fig. 6b. The galvanostatic charge/discharge (0.5–10 A/g) exhibited an approximately symmetrical triangular shape with

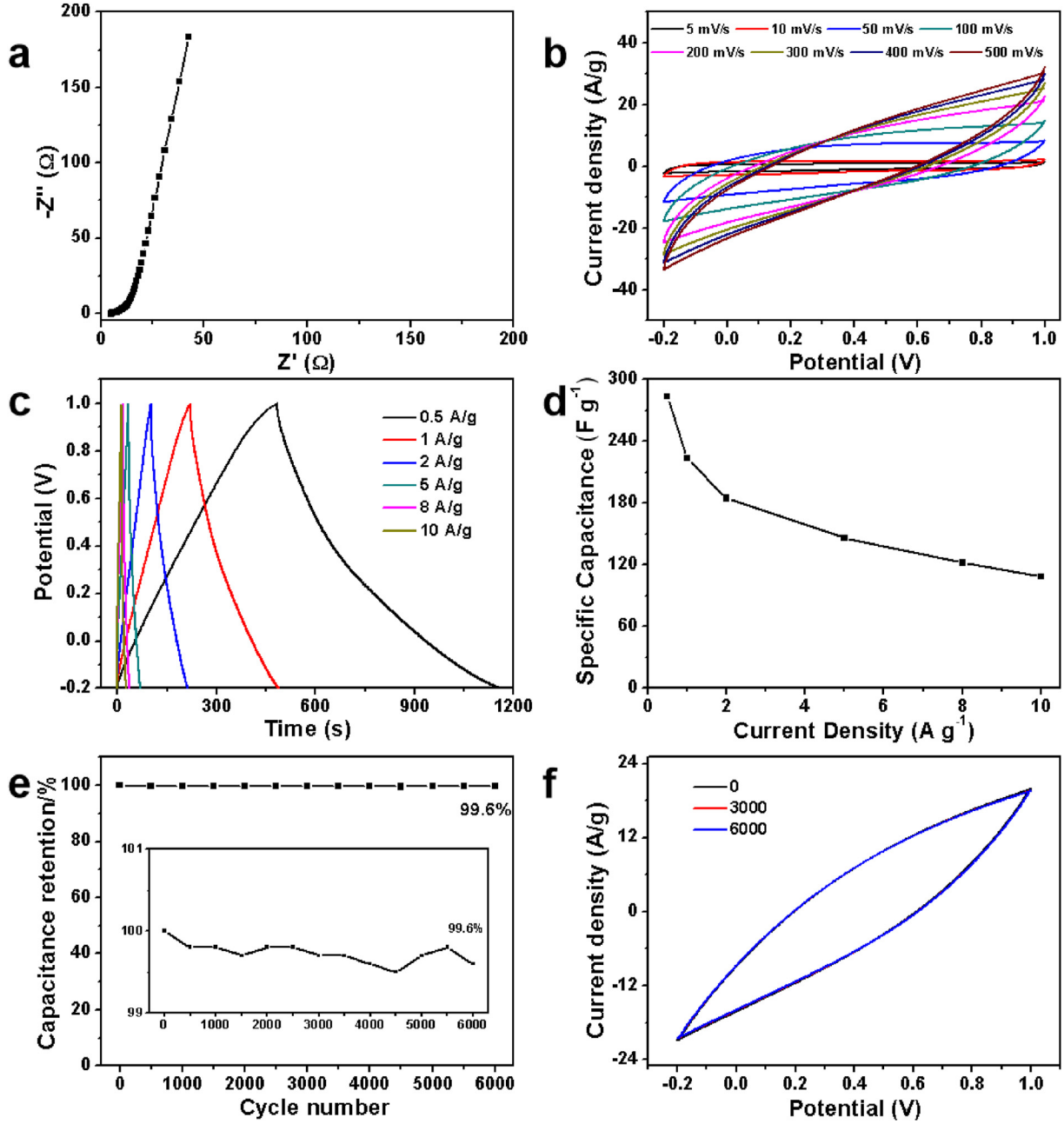

Fig. 6. Electrochemical performance of the PAN/γ-CD-MOF carbon membrane electrode. (a) Impedance spectra of the electrode. (b) CV curves of the electrode at various scan rates. (c) GCD profiles of the electrode at various current densities. (d) Specific capacitances of the electrode calculated from GCD profiles as a function of current density. (e) Cycling performance of the electrode at a scan rate of 200 mV/s. (f) CV curves of the electrode at the 1st, 3000th, and 6000th cycles.

slight nonlinearities, demonstrating its superior reversibility (Fig. 6c). According to the GCD curves, the maximum gravimetric capacitance of the PAN/γ-CD-MOF carbon membrane electrode reached 283.3 F/g at a current density of 0.5 A/g (Fig. 6d). Supplementary Table 2 compares the specific capacitance and cycle stability of PAN/γ-CD-MOF carbon membrane electrode with other reported electrodes in aqueous electrolyte. The results showed that PAN/γ-CD-MOF carbon membrane electrode achieved remarkable performance similar to or even better than that of the reported electrodes. The gravimetric capacitance of the PAN carbon membrane electrode was 174.7 F/g at a current density of 0.5 A/g (Supplementary Fig. 11), indicating that γ-CD-MOF played a vital role in increasing the electrode capacitance. PAN/γ-CD-MOF carbon membrane has a large specific surface area, porous structure, excellent conductivity, and nitrogen and oxygen doping, so that ions have faster diffusion and greater storage [21]. The cycling performance at a rate of 200 mV/s indicated that the PAN/γ-CD-MOF carbon membrane electrode retained 99.6% of the initial capacitance after 6000 cycles, presenting excellent long-term cycling stability (Fig. 6e and f).

2.5. Electrochemical behavior of PAN/γ-CD-MOF carbon membrane electrodes-SC

After individually testing the PAN/γ-CD-MOF carbon membrane as an electrode material, we assembled a symmetric

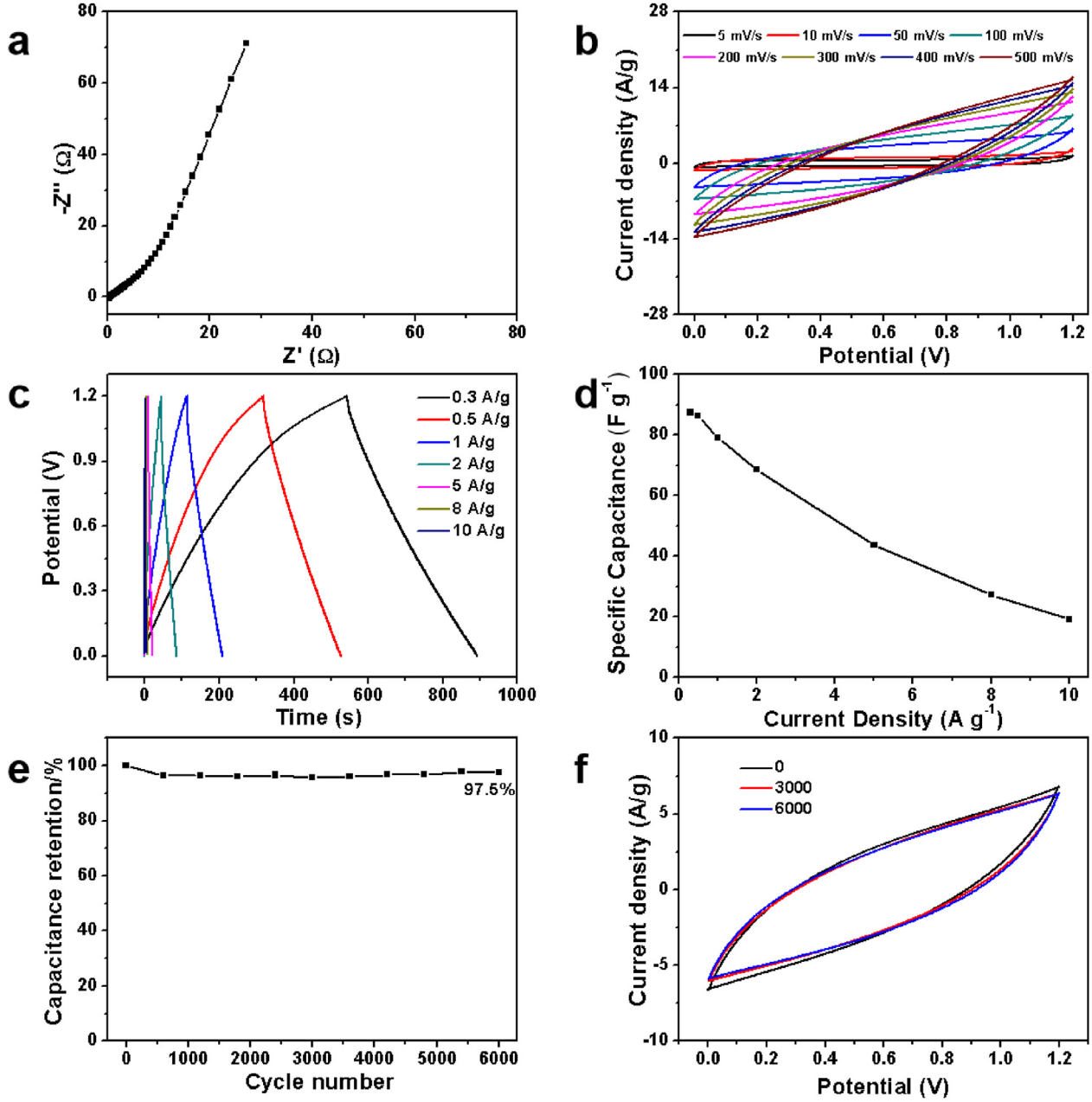

Fig. 7. Electrochemical behavior of the symmetric SC based on two PAN/γ-CD-MOF carbon membrane electrodes. (a) Impedance spectra of the symmetric SC. (b) CV curves of the symmetric SC at various scan rates. (c) GCD profiles of the symmetric SC at various current densities. (d) Specific capacitances of the symmetric SC calculated from GCD profiles as a function of current density. (e) Cycling performance of the symmetric SC at a scan rate of 200 mV/s. (f) CV curves of the electrode at the 1st, 3000th, and 6000th cycles.

supercapacitor using two PAN/γ-CD-MOF carbon membranes as additive/binder-free electrodes with a 1 M H_2SO_4 electrolyte. As presented in Fig. 7a, the electrolyte resistance was found to be 0.4 Ω, as obtained from the intercept in the high frequency region of the Nyquist plot. The charge transfer resistance was only 14.8 Ω, demonstrating amazing electron and ion transport capabilities. The above results, together with the straight line in the low frequency region, indicate a low internal resistance of the whole supercapacitor. Increasing the scan rate from 5 to 500 mV/s did not change the shape of the CV curve, indicating a high rate capability (Fig. 7b). GCD curves at various current densities from 0.3 to 10 A/g are shown in Fig. 7c. The energy density, power density and capacitance values calculated at various current densities are shown in Supplementary Table 3. The symmetric supercapacitor delivers a high specific capacitance of 86.4 F/g at 0.5 A/g (Fig. 7d). Significantly, our symmetric supercapacitor delivers a high energy density of 17.5 Wh/kg and power density of 6 kW/kg. The energy density, power density and cycle stability of PAN/γ-CD-MOF carbon membrane symmetric supercapacitor with other reported SCs were compared in Supplementary Table 4. These values are higher than those of most reported symmetrical SCs. Moreover, the symmetric supercapacitor displays an outstanding capacitance retention of 97.5% after 6000 charge/discharge cycles at 200 mV/s (Fig. 7e and f). The superior cycling ability of the SC is supported by its low equivalent series resistance.

3. Conclusion

In summary, we constructed a flexible PAN/γ-CD-MOF carbon membrane electrode through a very simple and convenient method of electrospinning PAN and K^+-γ-CD-MOF and then carbonizing. In light of large the specific surface area, porous structure, good conductivity and heteroatom doping, the electrode displayed a high capacity of 283.3 F/g and long cycling stability retained 99.6% of the initial capacitance after 6000 cycles. Then, two PAN/γ-CD-MOF carbon membrane electrodes were further used to assemble a symmetric supercapacitor, which showed advantageous features, such as a high energy density of 17.5 Wh/kg, a high power density of 6 kW/kg, and excellent durability with a capacitance retention of 97.5% after 6000 cycles. This work may inspire more efforts devoted to designing free-standing porous carbon flexible electrodes with higher specific capacities and to promoting the application of supramolecules in supercapacitors.

4. Experimental section

4.1. Reagents and materials

PAN (Mw = 150 kDa) and KAc were purchased from Heowns Biochem LLC. N, N-Dimethylformamide (DMF) and ethanol were purchased from Concord Technology (Tianjin) Co., Ltd. γ-Cyclodextrin was purchased from Kmart (Tianjin) Chemical Technology Co., Ltd. All chemicals and solvents were used as supplied.

4.2. Preparation of γ-CD-MOF

γ-CD-MOF was synthesized according to the reported literature with slight changes [47]. In detail, γ-CD and KAc aqueous solutions were mixed under continuous stirring for 1 h, and then the mixture was filtered through a 0.45 μm micro-porous membrane. After incubating for 6 h, ethanol was added. The obtained colorless crystals were washed with ethanol, and then dried in a vacuum oven at 45 °C for 24 h.

4.3. Preparation of PAN/γ-CD-MOF electrospun carbon membrane

Five milliliters of 10 w/v% PAN solution containing 0.25 g γ-CD-MOF was transferred to a 5 mL syringe with a 20-gauge (20 G) needle tip, and the spinning flow rate was 0.3 mm/min. A high voltage of 25 kV was applied, and the distance between the collector coated with aluminum foil and the needle tip was 20 cm. The collector was rotated at 40 rpm. The dry PAN/γ-CD-MOF nanofibrous membrane was collected directly from aluminum foil. γ-CD-MOF is beneficial for increasing the micropore content, but if too much γ-CD-MOF was added to PAN, the needle would be blocked, and electrospinning could not be carried out. After electrospinning, the PAN/γ-CD-MOF nanofibrous membrane was calcined at 900 °C in N_2 for 3 h with a heating rate of 2.5 °C/min to obtain a PAN/γ-CD-MOF carbon membrane.

4.4. Material characterizations

The surface morphology and elemental analysis of the samples were acquired by using an SEM (MERLIN Compact, Germany) equipped with an X-ray energy spectrometer. All samples were vacuum-dried and then coated with gold before examination. Transmission electron microscopy (TEM) images were taken on a Philips Tecnai G2 F20 microscope. FTIR analysis was performed by a spectrometer (Bruker-TENSOR II, Germany) to analyze the functional groups between 4000 and 400 cm^{-1}. The surface chemical composition of the nanofibrous membranes was studied via XPS. XPS data were collected by an instrument (Kratos Analytical Ltd.-Axis Ultra DLD) under ultrahigh vacuum equipping with a monochromatized Al Kα X-ray source, and analyzed with CASAXPS software. X-ray diffraction (XRD) patterns from 3° to 80° were recorded on a Rigaku SmartLab (Japan) diffractometer using Cu Kα radiation. The nitrogen sorption isotherms and pore size distributions of the samples were measured at liquid nitrogen temperatures using an automatic gas adsorption analyzer (Autosurb IQ, USA). The surface area of the samples was determined using the BET equation, and pore size distributions were calculated using the density functional theory method. Thermal gravimetric analyses (TGA) were carried out on a thermogravimetric analyzer (NETZSCH, Germany) in the temperature range from 25 to 900 °C at a heating rate of 10 °C/min under a purified nitrogen gas flow of 25 mL/min. The graphitization degrees of the PAN/γ-CD-MOF carbon membrane were checked by Raman spectrometry performed on a Renishaw inVia Reflex with an excitation wavelength of 532 nm at room temperature.

4.5. Electrochemical properties of the electrospun nanofibrous membrane

The electrochemical performances, including electrochemical impedance spectroscopy (EIS), cyclic voltammetry (CV), and galvanostatic charge/discharge (GCD) measurements, were employed with an electrochemical workstation (Chenhua, CHI 660E). All of the electrochemical performances of the electrode were studied in a three-electrode configuration in 1 M H_2SO_4 electrolyte, with the electrospun carbon membrane, Ag/AgCl and Pt plate serving as the working electrode, reference electrode and counter electrode, respectively. EIS data were collected in a frequency range from 10^5 Hz to 0.1 Hz at a potentiostatic signal amplitude of 5 mV. CV experiments were performed at different sweep rates of 5−500 mV/s. GCD tests were performed at various current densities from 0.5 to 10 A/g. The cycling stability of the electrodes and symmetrical supercapacitor were determined by repeating the CV experiments at 200 mV/s. After the electrode performance tests, two pieces of carbon nanofibrous membranes were directly used as the electrodes for a two-electrode symmetrical supercapacitor without any binders or supports. The potential window was −0.2−1 V for electrode performance tests, and 0−1.2 V for supercapacitor performance tests.

Calculations: The gravimetric capacitance (C, F g^{-1}) was calculated from the GCD curves according to the following Eq. (1) [22], where I/m is the current density (A g^{-1}), t is the discharge time (s), and v is the voltage range (V).

$$C = I/m \times t/v \tag{1}$$

The energy density (E, Wh kg^{-1}) was calculated from Eq. (2) [22], where C is the gravimetric capacitance, and ΔV is the discharge voltage range (V).

$$E = 1/2 \times C \times (\Delta V)^2 / 3.6 \tag{2}$$

The power density (P, W kg^{-1}) was calculated from Eq. (3) [22], where E is the energy densities and Δt is discharge time (s).

$$P = E/\Delta t \times 3600 \tag{3}$$

Credit author statement

Wenshi Xu: Conceptualization, Investigation, Methodology, Writing − original draft, Data curation. Li-Hua Wang: Supervision. Yong Chen: Methodology, Review, Supervision. Yu Liu: Conceptualization, Review, Supervision.

Declaration of competing interest

The authors declare that they have no known competing financial interests or personal relationships that could have appeared to influence the work reported in this paper.

Acknowledgements

We thank the National Natural Science Foundation of China (grant nos. 22131008 and 21971127) and the Haihe Laboratory of Sustainable Chemical Transformations for financial support.

Appendix A. Supplementary data

Supplementary data to this article can be found online at https://doi.org/10.1016/j.mtchem.2022.100896.

References

[1] N. Lima, A.C. Baptista, B.M.M. Faustino, S. Taborda, A. Marques, I. Ferreira, Carbon threads sweat-based supercapacitors for electronic textiles, Sci. Rep. 10 (2020) 7703, https://doi.org/10.1038/s41598-020-64649-2.
[2] H. Lee, G. Jung, K. Keum, J.W. Kim, H. Jeong, Y.H. Lee, D.S. Kim, J.S. Ha, A textile-based temperature-tolerant stretchable supercapacitor for wearable electronics, Adv. Funct. Mater. 31 (2021) 2106491, https://doi.org/10.1002/adfm.202106491.
[3] Z. Wen, M.-H. Yeh, H. Guo, J. Wang, Y. Zi, W. Xu, J. Deng, L. Zhu, X. Wang, C. Hu, L. Zhu, X. Sun, Z.L. Wang, Self-powered textile for wearable electronics by hybridizing fiber-shaped nanogenerators, solar cells, and supercapacitors, Sci. Adv. 2 (2016), e1600097, https://doi.org/10.1126/sciadv.1600097.
[4] J. Li, S. Luo, G. Liu, J. Wan, J. Lu, B. Li, X. Han, C. Hu, A high-performance asymmetric supercapacitor achieved by surface-regulated MnO_2 and organic-framework-derived N-doped carbon cloth, Mater. Today Chem. 22 (2021) 100620, https://doi.org/10.1016/j.mtchem.2021. 100620.
[5] C. Gao, J. Huang, Y. Xiao, G. Zhang, C. Dai, Z. Li, Y. Zhao, L. Jiang, L. Qu, A seamlessly integrated device of micro-supercapacitor and wireless charging with ultrahigh energy density and capacitance, Nat. Commun. 12 (2021) 2647, https://doi.org/10.1038/s41467-021-22912-8.
[6] J. Park, D.B. Ahn, J. Kim, E. Cha, B.-S. Bae, S.-Y. Lee, J.-U. Park, Printing of wirelessly rechargeable solid-state supercapacitors for soft, smart contact lenses with continuous operations, Sci. Adv. 5 (2019), eaay0764, https://doi.org/10.1126/sciadv.aay0764.
[7] H. Sheng, J. Zhou, B. Li, Y. He, X. Zhang, J. Liang, J. Zhou, Q. Su, E. Xie, W. Lan, K. Wang, C. Yu, A thin, deformable, high-performance supercapacitor implant that can be biodegraded and bioabsorbed within an animal body, Sci. Adv. 7 (2021), eabe3097, https://doi.org/10.1126/sciadv.abe3097.
[8] R.N. Bulakhe, S.A. Arote, B. Kwon, S. Park I, In, Facile synthesis of nickel cobalt sulfide nano flowers for high performance supercapacitor applications, Mater. Today Chem. 15 (2020) 100210, https://doi.org/10.1016/j.mtchem.2019.100210.
[9] H. Shao, Y.-C. Wu, Z. Lin, P.-L. Taberna, P. Simon, Nanoporous carbon for electrochemical capacitive energy storage, Chem. Soc. Rev. 49 (2020) 3005–3039, https://doi.org/10.1039/d0cs00059k.
[10] J. Ji, W. Wu, W. Liang, G. Cheng, R. Matsushita, Z. Yan, X. Wei, M. Rao, D.-Q. Yuan, G. Fukuhara, T. Mori, Y. Inoue, C. Yang, An ultimate stereocontrol in supramolecular photochirogenesis: photocyclodimerization of 2-anthracenecarboxylate mediated by sulfur-linked β-cyclodextrin dimers, J. Am. Chem. Soc. 141 (2019) 9225–9238, https://doi.org/10.1021/jacs.9b01993.
[11] J. Yao, H. Mizuno, C. Xiao, W. Wu, Y. Inoue, C. Yang, G. Fukuhara, Pressure-driven, solvation-directed planar chirality switching of cyclophano-pillar[5] arenes (molecular universal joints), Chem. Sci. 12 (2021) 4361–4366, https://doi.org/10.1039/d0sc06988d.
[12] G. Sun, W. Qian, J. Jiao, T. Han, Y. Shi, X.-Y. Hu, L. Wang, A highly efficient artificial light-harvesting system with two-step sequential energy transfer based on supramolecular self-assembly, J. Mater. Chem. A. 8 (2020) 9590–9596, https://doi.org/10.1039/d0ta03169k.
[13] Q. Lin, L. Li, M. Tang, S. Uenuma, J. Samanta, S. Li, X. Jiang, L. Zou, K. Ito, C. Ke, Kinetic trapping of 3D-printable cyclodextrin-based poly(pseudo)rotaxane networks, Chem. 7 (2021) 2442–2459, https://doi.org/10.1016/j.chempr.2021.06.004.
[14] Z. Liu, X. Dai, Y. Sun, Y. Liu, Organic supramolecular aggregates based on water-soluble cyclodextrins and calixarenes, Aggregate 1 (2020) 31–44, https://doi.org/10.1002/agt2.3.
[15] W. Xu, Y. Chen, B. Zhang, W. Xu, J. Niu, Y. Liu, Supramolecular assembly of beta-cyclodextrin-modified polymer by electrospinning with sustained antibacterial activity, Biomacromolecules 22 (2021) 4434–4445, https://doi.org/10.1021/acs.biomac.1c01007.
[16] S. Cao, H. Zhang, Y. Zhao, Y. Zhao, Pillararene/calixarene-based systems for battery and supercapacitor applications, eScience (2021), https://doi.org/10.1016/j.esci.2021.10.001.
[17] J. Kim, J.W. Kim, S. Kim, K. Keum, J. Park, Y.R. Jeong, S.W. Jin, J.S. Ha, Stretchable, self-healable, and photodegradable supercapacitor based on a polyelectrolyte crosslinked via dynamic host-guest interaction, Chem. Eng. J. 422 (2021) 130121, https://doi.org/10.1016/j.cej.2021.130121.
[18] L. Feng, S.S. Jia, Y. Chen, Y. Liu, Highly elastic slide-ring hydrogel with good recovery as stretchable supercapacitor, Chem. Eur. J. 26 (2020) 14080–14084, https://doi.org/10.1002/chem.202001729.
[19] S.-S. Jia, W.-S. Xu, Y. Chen, Y. Liu, Pyrrole/macrocycle/MOF supramolecular co-assembly for flexible solid state supercapacitors, Chin. Chem. Lett. 32 (2021) 2773–2776, https://doi.org/10.1016/j.cclet.2021.03.002.
[20] H. Qiu, H. Cheng, J. Meng, G. Wu, S. Chen, Magnetothermal microfluidic-assisted hierarchical microfibers for ultrahigh-energy-density supercapacitors, Angew. Chem. Int. Ed. 59 (2020) 7934–7943, https://doi.org/10.1002/ange.202000951.
[21] H. Cheng, J. Meng, G. Wu, S. Chen, Hierarchical micro-mesoporous carbon-framework-based hybrid nanofibres for high-density capacitive energy storage, Angew. Chem. Int. Ed. 58 (2019) 17465–17473, https://doi.org/10.1002/anie.201911023.
[22] K. Jayaramulu, M. Horn, A. Schneemann, H. Saini, A. Bakandritsos, V. Ranc, M. Petr, V. Stavila, C. Narayana, B. Scheibe, S. Kment, M. Otyepka, N. Motta, D. Dubal, R. Zboril, R.A. Fischer, Covalent graphene-MOF hybrids for high-performance asymmetric supercapacitors, Adv. Mater. 33 (2021) 2004560, https://doi.org/10.1002/adma.202004560.
[23] D.M. Reinoso, U. Diaz, M.A. Frechero, Structural study of functional hierarchical porous carbon synthesized from metal-organic framework template, Mater. Today Chem. 14 (2019) 100188, https://doi.org/10.1016/j.mtchem.2019.08.007.
[24] J. Yan, K. Dong, Y. Zhang, X. Wang, A.A. Aboalhassan, J. Yu, B. Ding, Multifunctional flexible membranes from sponge-like porous carbon nanofibers with high conductivity, Nat. Commun. 10 (2019) 5584, https://doi.org/10.1038/s41467-019-13430-9.
[25] Z. Zhou, T. Liu, A.U. Khan, G. Liu, Block copolymer-based porous carbon fibers, Sci. Adv. 5 (2019), https://doi.org/10.1126/sciadv.aau6852 eaau6852.
[26] K. Li, B. Zhao, H. Zhang, H. Lv, J. Bai, H. Ma, P. Wang, W. Li, J. Si, X. Zhu, Y. Sun, 3D porous honeycomb-like CoN-Ni_3N/N-C nanosheets integrated electrode for high-energy-density flexible supercapacitor, Adv. Funct. Mater. 31 (2021) 2103073, https://doi.org/10.1002/adfm.202103073.
[27] A. Sarno, L. Baldino, C. Scudieri, S. Cardea, E. Reverchon, A one-step SC-CO_2 assisted technique to produce compact PVDF-HFP MoS_2 supercapacitor device, J. Phys. Chem. Solids 136 (2020) 109132, https://doi.org/10.1016/j.jpcs.2019.109132.
[28] C. Zhao, X. Sun, W. Li, M. Shi, K. Ren, X. Lu, Reduced self-discharge of supercapacitors using piezoelectric separators, ACS Appl. Energy Mater. 4 (2021) 8070–8075, https://doi.org/10.1021/acsaem.1c01373.
[29] W. Zhang, S. Wei, Y. Wu, Y.-L. Wang, M. Zhang, D. Roy, H. Wang, J. Yuan, Q. Zhao, Poly(Ionic liquid)-derived graphitic nanoporous carbon membrane enables superior supercapacitive energy storage, ACS Nano 13 (2019) 10261–10271, https://doi.org/10.1021/acsnano.9b03514.
[30] S. Zhang, H. Liu, J. Yu, B. Li, B. Ding, Multi-functional flexible 2D carbon nanostructured networks, Nat. Commun. 11 (2020) 5134, https://doi.org/10.1038/s41467-020-18977-6.
[31] D. Shen, J.A. Cooper, P. Li, Q.-H. Guo, K. Cai, X. Wang, H. Wu, H. Chen, L. Zhang, Y. Jiao, Y. Qiu, C.L. Stern, Z. Liu, A.C.H. Sue, Y.-W. Yang, F.M. Alsubaie, O.K. Farha, J.F. Stoddart, Organic counteranion Co-assembly strategy for the formation of gamma-cyclodextrin-containing hybrid frameworks, J. Am. Chem. Soc. 142 (2020) 2042–2050, https://doi.org/10.1021/jacs.9b12527.
[32] H.A. Patel, T. Islamoglu, Z. Liu, S.K.M. Nalluri, A. Samanta, O. Anamimoghadam, C.D. Malliakas, O.K. Farha, J.F. Stoddart, Noninvasive substitution of K^+ sites in cyclodextrin metal-organic frameworks by Li^+ ions, J. Am. Chem. Soc. 139 (2017) 11020–11023, https://doi.org/10.1021/jacs.7b06287.
[33] Y. Chen, B. Yu, Y. Cui, S. Xu, J. Gong, Core-shell structured cyclodextrin metal-organic frameworks with hierarchical dye encapsulation for tunable light emission, Chem. Mater. 31 (2019) 1289–1295, https://doi.org/10.1021/acs.chemmater.8b04126.
[34] O. Mehmood, S. Farrukh, A. Hussain, A. Rehman, Y. Liu, S. Butt, E. Pervaiz, Optimization analysis of polyurethane based mixed matrix gas separation membranes by incorporation of gamma-cyclodextrin metal organic frame work, Chem. Pap. 74 (2020) 3527–3543, https://doi.org/10.1007/s11696-020-01179-1.
[35] I. Kritskiy, T. Volkova, A. Surov, I. Terekhova, gamma-Cyclodextrin-metal organic frameworks as efficient microcontainers for encapsulation of leflunomide and acceleration of its transformation into teriflunomide, Carbohydr. Polym. 216 (2019) 224–230, https://doi.org/10.1016/j.carbpol.2019.04.037.
[36] I. Kritskiy, T. Volkova, T. Sapozhnikova, A. Mazur, P. Tolstoy, I. Terekhova, Methotrexate-loaded metal-organic frameworks on the basis of gamma-cyclodextrin: design, characterization, in vitro and in vivo investigation, Mat. Sci. Eng. C 111 (2020) 110774, https://doi.org/10.1016/j.msec.2020.110774.
[37] W. Xu, Y. Chen, W. Xu, X. Wu, Y. Liu, Electrospinning oriented self-cleaning porous crosslinking polymer for efficient dyes removal, Adv. Mater. Interfaces 7 (2020) 2001050, https://doi.org/10.1002/admi.202001050.

[38] W. Xu, Y. Chen, Y. Liu, Directional water transfer janus nanofibrous porous membranes for particulate matter filtration and volatile organic compound adsorption, ACS. Appl. Mater. Interfaces 13 (2021) 3109–3118, https://doi.org/10.1021/acsami.0c18526.
[39] R.A. Smaldone, R.S. Forgan, H. Furukawa, J.J. Gassensmith, A.M.Z. Slawin, O.M. Yaghi, J.F. Stoddart, Metal-organic frameworks from edible natural products, Angew. Chem. Int. Ed. 49 (2010) 8630–8634, https://doi.org/10.1002/anie.201002343.
[40] C. Cui, Y. Gao, J. Li, C. Yang, M. Liu, H. Jin, Z. Xia, L. Dai, Y. Lei, J. Wang, S. Wang, Origins of boosted charge storage on heteroatom-doped carbons, Angew. Chem. Int. Ed. 59 (2020) 7928–7933, https://doi.org/10.1002/anie.202000319.
[41] G. Wang, S.-K. Kim, M.C. Wang, T. Zhai, S. Munukutla, G.S. Girolami, P.J. Sempsrott, S. Nam, P.V. Braun, J.W. Lyding, Enhanced electrical and mechanical properties of chemically cross-linked carbon-nanotube-based fibers and their application in high-performance supercapacitors, ACS Nano 14 (2019) 632–639, https://doi.org/10.1021/acsnano.9b07244.
[42] J. Lu, X. Sui, B. Yang, J. Chen, L. Cai, W. Li, M. Jiang, S. Hao, Ultrafast in-situ transformation of graphite into graphene nanosheets by high current pulsed electron beam direct irradiation, Appl. Surf. Sci. 572 (2021) 151498, https://doi.org/10.1016/j.apsusc.2021. 151498.
[43] M.R. Benzigar, S.N. Talapaneni, S. Joseph, K. Ramadass, G. Singh, J. Scaranto, U. Ravon, K. Al-Bahily, A. Vinu, Recent advances in functionalized micro and mesoporous carbon materials: synthesis and applications, Chem. Soc. Rev. 47 (2018) 2680–2721, https://doi.org/10.1039/c7cs00787f.
[44] H. Bi, X. Wang, H. Liu, Y. He, W. Wang, W. Deng, X. Ma, Y. Wang, W. Rao, Y. Chai, H. Ma, R. Li, J. Chen, Y. Wang, M. Xue, A universal approach to aqueous energy storage via ultralow-cost electrolyte with super-concentrated sugar as hydrogen-bond-regulated solute, Adv. Mater. 32 (2020) 2000074, https://doi.org/10.1002/adma.202000074.
[45] J. Shang, Q. Huang, L. Wang, Y. Yang, P. Li, Z. Zheng, Soft hybrid scaffold (SHS) strategy for realization of ultrahigh energy density of wearable aqueous supercapacitors, Adv. Mater. 32 (2020) 1907088, https://doi.org/10.1002/adma.201907088.
[46] T. Wu, X. Wu, L. Li, M. Hao, G. Wu, T. Zhang, S. Chen, Anisotropic boron-carbon hetero-nanosheets for ultrahigh energy density supercapacitors, Angew. Chem. Int. Ed. 59 (2020) 23800–23809, https://doi.org/10.1002/anie.202011523.
[47] H. Ding, L. Wu, T. Guo, Z. Zhang, B.M. Garba, G. Gao, S. He, W. Zhang, Y. Chen, Y. Lin, H. Liu, J. Anwar, J. Zhang, CD-MOFs crystal transformation from dense to highly porous form for efficient drug loading, Cryst. Growth. Des. 19 (2019) 3888–3894, https://doi.org/10.1021/acs.cgd.9b00319.